Corrosion behavior of the resistance sintered TiAl based intermetallics induced by two different molten salt mixture

Y. Garip, O. Ozdemir

Sakarya Applied Science University, Technology Faculty, Department of Metallurgy and Materials Engineering,

Esentepe Campus, 54187, Sakarya-Turkey

*Corresponding author.

E-mail address: yigitgarip@hotmail.com (Y. Garip).

Highlights

- The RS technique was used in the preparation of TiAl based alloys.
- The effect of Cr, Mn and Mo alloying elements on the cyclic hot corrosion behaviors of TiAl based intermetallics is investigated.
- Cr and Mn are found to be beneficial to the corrosion resistance.
- Mo addition was detrimental for hot corrosion resistance of the TiAl based intermetallics due to the alloy-induced acidic fluxing.
- NaCl-containing salt mixture caused severe degradation in the samples due to the self-sustaining reaction mechanism.

Abstract

The cyclic hot corrosion behaviors of TiAl based intermetallics were studied in two different molten salts consisting of % wt. Na_2SO_4-25NaCl and Na_2SO_4-25K_2SO_4 at 800 and 900°C for 180h, respectively. The aim of the study is to elucidate the effect of alloying elements on hot corrosion phenomena in the corrosive molten salt mixture. Corrosion kinetics revealed the Mo-added samples exhibit poor corrosion resistance in both corrosive salt mixture. It has been found that the NaCl-containing salt mixture clearly influence the extent of degradation due to the self-sustaining reaction mechanism.

Keywords: Ti-Al, Aluminides, Hot corrosion, Alloying elements, Resistance sintering

1. Introduction

Components of gas turbine engines (like turbine blades, disks, stator blades, guide vanes and rotors) used in aerospace, marine and industrial applications must be able to withstand many harsh conditions, including cyclic stresses in oxidizing and/or corrosive environments during operation at elevated temperatures [1-3]. Extensive studies have carried out on the reduction of NOx emission gases and low fuel consumption to provide higher efficiency of gas turbine engines. This can be achieved in two ways: the first one is increasing the combustion temperature and pressure in the gas turbine, and the second one is applying developments in cooling systems. However, higher service temperatures expose components to high-temperature corrosion and thus considerably decrease their service life [4]. The γ-TiAl based intermetallic compounds have drawn attention materials for high-temperature applications due to a combination of superior features such as high melting point, lower density, adequate high specific strength and elastic modulus as well as good oxidation and corrosion resistance [5-9]. The efforts to develop titanium aluminides have led the use of these aluminides as low-pressure turbine (LPT) blades in GEnx ™ 1B (Boeing 787) and the GEnx ™ 2B (Boeing 747-8) engines [10,11]. Furthermore, γ-TiAl based intermetallics are lighter than nickel-based superalloys and offer the opportunity of weight-saving up to 50% for the hot sections of the gas turbine, resulting in engine weight reduction, performance enhancement and reduction of the centrifugal force applied to the turbine disk [11-13].

During the combustion of a gas turbine engine, the hot section components can expose to an aggressive form of corrosion related to the presence of condensing various salts (e.g., Na_2SO4, K_2SO_4, NaCl, V_2O_5) on the external surface of components or oxide scales. This type of corrosion, causing the degradation of materials, is called hot corrosion [1,4,6,14]. The deposition of fused salts results from infiltrated air and residual fuels in gas turbine engines [15]. The high concentrations of sulfur (wt.% 4), sodium (wt.% 0.01) and vanadium (0.05 wt.%) are the results of low-quality fuel. These impurities and the chlorine from ingested air react with the oxygen surrounding the hot-section region (combustion chambers and turbine blades) and form mostly volatile oxides such as SO_2, SO_3, NaOH, NaO, Na_2O, $VO(OH)_3$, V_2O_5 and V_2O_4. The mentioned compounds condense at the temperatures range from 500 to 900°C to form molten salt deposits [16].

There are various processing techniques to produce TiAl alloys, such as vacuum arc melting [17,18], hot isostatic pressing [19] and hot press sintering [20]. However, the manufacturing costs are high due to the several problems in casting processes, as an example, considerable effort has been devoted to minimizing the composition segregation and texture during solidification [21]. Besides, the TiAl alloys have a low castability, large solidification shrinkage rate and high chemical reactivity, resulting in misrun defects on the surface, porosity and crack [22]. The above considerations have restricted the applications of these alloys in the industrial area. Therefore, scientists and engineers are faced with the fact of finding alternative processes to conventional methods to produce TiAl based alloys. It was reported that the coarse lamellar structures and segregation faced by the casting alloys could be prevented by using the powder metallurgy route with rapid solidification [23]. The resistance sintering (RS) technique has been attracted attention as a new powder metallurgy approach for producing intermetallics, ceramics and composites materials. The RS process is regarded as an ever-growing and effective producing technology. The most significant property of the RS is that the powder or green compact are heated by the Joule effect and thus, the materials can be synthesized uniformly and rapidly. As a result, materials with high dense and fine microstructure can be achieved in very short processing time [6,24,25].

TiAl alloys inevitably suffer severe hot corrosion in the actual environment. That is to say, it is important to investigate the corrosion resistance of TiAl in the molten salt environments. However, very little amount of research has been focused on the hot corrosion behavior of TiAl and reported in the literature. In view of this, the present study was undertaken. Thus, the aim of this study is to investigate cyclic hot corrosion behavior of TiAl based intermetallics produced by RS technique in two different molten salts consisting of wt.% Na_2SO_4-25K_2SO_4 and Na_2SO_4-25NaCl.

2. Experimental procedure

2.1. Sample preparation

Titanium aluminides used in this study have the nominal composition of (at.%) Ti-48Al, Ti-48Al-2Cr, Ti-48Al-2Mn, Ti-48Al-2Cr-2Mo and Ti48Al-2Mn-2Mo were prepared by RS technique. The elemental materials used in the present study were titanium (purity 99.5 %, 40 µm), aluminum (purity 99.5 %, 7-15 µm), chromium (purity 99.2 %, 10 µm), molybdenum (purity 99.55 %, 3-7µm) and manganese (purity 99.6 %, 10 µm).

All elemental powders were provided by Alfa Aesar company. Prior to the RS process, the powders were weighed according to the nominal compositions and then blended into a mechanical mixer for 4 hours to obtain a homogenous powder mixture. The mechanical mixer parameters are as follows; ball-to-powder weight ratio (BPR) was 8:1 and the rotation speed was 210 r/min. The mixed powders of 5 g were inserted into a steel die with an inner diameter of 20 mm. A uniaxial mechanical load of 100 MPa for 1 min. was applied to compact the mixed powders in the die. Afterwards, the compacted powders placed between two counter-sliding punches were synthesized at 4800 amperes and 60 MPa for 35 minutes by RS in air. The electric current applied simultaneously with a uniaxial mechanical load was maintained at the set value throughout RS process. After the sintering, the sintered sample in the die was got using a uniaxial load and then air-cooled to ambient temperature. Finally, the sintered sample with dimensions of Ø 20 mm x 5 mm was obtained. The sintering current profile and pressure conditions of RS process are shown in Fig. 1.

Figure 1

2.2. Hot corrosion test

Before the hot corrosion test, the original surface area of each samples were identified using the Solidworks and then weighed by an electronic scales with an accuracy of 10^{-2} mg. In this study, wt.% Na_2SO_4-25K_2SO_4 and Na_2SO_4-25NaCl salt mixtures were used to simulate conditions similar to the actual environment as it is a eutectic composition, having melting points about 825 and 630°C, respectively. These conditions in combination with cyclic heating would provide that the salt melts and occurs a severe corrosion medium for interaction with the alloy. The samples were immersed completely in an alumina crucible with the same amount of mixed salts during the whole corrosion process. A separate alumina crucible was used for each sample during the hot corrosion test. These crucibles prior to carrying out of the experiment were heated at 950°C for 1 h so as to remove moisture from the crucibles. The hot corrosion testing was carried out in an electric resistance furnace at 800 and 900°C (depends on the salt composition) for 180 h and 15 cycles. A cycle involves heating the samples to the test temperature and holding them in the furnace for 12 h. At the end of the cycle, the samples were removed from the furnace and then air cooled in room temperature. After being cooled, they were washed in distilled water at 100°C for 10 min to remove residual salts on the surfaces and then dried by using air flow. Afterwards, the samples were again weighed to evaluate the corrosion kinetic. To ensure the accuracy of the experiment, each sample was weighed four times at one cycle and the results were averaged

to obtain the effective weight change values. The deviation of each measurement was found to be within 8% error range. For the next cycle, the samples were re-buried in the crucibles consisting the same amount of salt and composition. This procedure was reapplied for each HC cycle.

2.3. Characterization

In order to perform the SEM studies, the sintered samples were gradually grounded by SiC papers up to 1200 and subsequently polished using 1 μm diamond particles. The samples were etched by a Kroll reagent: 3 vol. % HF, 5 vol. % HNO_3, 92 vol. % distilled water.

X-ray diffraction analysis (Rigaku, D/MAX-B/2200/PC) was employed to identify the phase constitution of the samples and corrosion products using diffractometer with Cu Kα radiation and operated at 20 kV. The XRD data scanning angle 2θ range from 20° to 90° with a step size of 0.02°. The initial microstructures of the samples, the surface morphology and the cross-sectional microstructure of the corroded samples were observed by a scanning electron microscopy (SEM, JEOL JSM-6060, LV). Chemical compositions of the present phases were examined by energy-dispersive spectroscopy (EDS, IXRF 5000). The relative densities of the samples were calculated by Archimedes' principle, based on the immersion technique in distilled water. The microhardness of the samples was determined using Vickers diamond indenter. For each samples, 4 measurements were conducted using the application of a load of 200 g for dwell time of 10 secs. and measurements were averaged.

3. Results

3.1. Characterization of the RSed intermetallics

Titanium and aluminium may react during the sintering in the following manner [26]:

$$Ti + 3Al = TiAl_3 \quad (2)$$

$$4Ti + TiAl_3 = 2TiAl + Ti_3Al \quad (3)$$

In the first stage, Al and Ti react to form $TiAl_3$ which is an intermediate phase, under the melting point of Al (~600°C). It was reported that the free energy of $TiAl_3$ is the lowest in comparison to Ti_3Al and TiAl phases in all temperatures. It is thus expected that the first product to be developed will be $TiAl_3$ phase during sintering. Besides, since the diffusion rate of Al in $TiAl_3$ phase is higher compared to other phases, it is more stable at low temperatures [26]. Additionally, melting of aluminum during sintering leads to an increase in its diffusion

rate [27]. In the second stage (Eq. 3), TiAl and Ti_3Al phases are formed by the interaction of Ti_3Al and Ti (remaining) at high temperatures.

The generation of TiAl and Ti_3Al phases in accordance with the Eqs. (2 and 3) was supported by XRD patterns (Fig. 2). This indicates that the electric current applied during the RS promotes the phase formation process in the Ti-Al system. The $TiAl_3$ which is an intermediate phase was not found in the XRD patterns, showing that the applied electric current and sintering time were adequate. Tamburini et al. [28] studied the effect of the current on the growth kinetics of the product phase in the Mo-Si system and found that a remarkable promotion in the rate of growth during applying the electric current.

Figure 2

According to XRD results (Fig. 2), the intermetallics consisted of α_2-Ti_3Al and γ-TiAl phases. For many years, the researchers have focused on TiAl alloys with two-phase (γ-TiAl/α_2-Ti_3Al). The reason is that the two mentioned phases alloy exhibit desirable mechanical features [8]. Figure 2 shows that phase components of intermetallics were not changed by the added alloying elements. The SEM images of the RSed samples are presented in Fig. 3. The EDS analysis results (at.%) of spots shown in Fig. 3 are presented in Table 1.

Figure 3

Figure 3 shows that the microstructures of Ti-48Al, Ti-48Al-2Cr and Ti-48Al-2Mn samples were composed of two different phase areas as gray tone and dark-gray tone. It was observed that a bright phase in addition to TiAl and Ti_3Al phases in the Mo-added samples. When considering the results of EDS analysis in Table 1, the gray phase (spots 1,3,7,8,12) was found to be an α_2-Ti_3Al phase, the dark-gray phase (spots 2,4,6,9,11) was found to be a γ-TiAl phase and the bright phase (spots 5 and 10) was found to be Mo-rich γ-TiAl phase.

Table 1

The densities of the samples calculated according to the Archimedes' principle and presented in Table 2. Since the chemical composition changes the density of alloy, the densities of γ-TiAl and α_2-Ti_3Al are between 3.7-3.9 and 4.1-4.7 g/cm^3, respectively [29]. As can be seen in Fig. 3, the samples were made up of γ-TiAl and α_2-Ti_3Al phases. It is thus expected that the experimental densities were also to be in the range of the density values of the mentioned two phases. It can be noticed that the relative densities of Mo-free samples were higher in comparison to other samples. One of the main reasons for the use of RS is to avoid grain

growth in the final microstructure of alloys because rapid heating is an effective way of improving densification while simultaneously suppressing grain growth.

In a study done by Xu et al. [30], the alternating current-assisted sintering (ACS) and conventional pressureless sintering (PS) methods were used to prepare Al_2O_3 ceramics. The authors showed that the density of the ACSed sample was 3.81 g/cm^3 at 1400°C for dwelling time of 5 min, while the density of the PSed sample was 3.77 g/cm^3 at 1500°C for dwelling time of 1 h. In addition, the flexural strength of the ACSed sample was more than 50% higher than that of the PSed sample. They proposed that the mechanical pressure and high heating rate applied in the ACS method play a crucial role in decreasing the sintering temperature and enhancing the densification process.

Table 2

When the powder metallurgy technique is used to prepare TiAl alloys, the Kirkendall effect occurs during sintering since there is a great difference between the Al and Ti diffusion rate. When the sintering pressure is not used during process, surface cracking and swelling may take place in the alloy as a result of the generation of Kirkendall pores [31]. However, it was not observed that the surface cracking or swelling due to the fact that in the used method in this study sintering pressure and electric current are applied simultaneously. Table 3 showed the microhardness values of the samples. It can be seen that Cr, Mn and Mo alloying elements give rise to a small increase in the hardness. These obtained results are consistent with those reported by other authors [32,33].

Table 3

3.2. Hot corrosion behavior

Hot corrosion kinetics of the samples in the different molten salt mixture are presented in Fig. 4. The weight change per unit area was calculated by dividing the weight difference of the samples weighed before and after corrosion (m_2-m_1) with the surface area of the sample. The hot corrosion kinetics of the samples were determined by the following equation:

$$\Delta W = \frac{(m_2\text{-}m_1)}{A} \qquad (4)$$

where ΔW presents the weight change per unit area (mg/cm^2), m_1 presents the initial weight (mg), m_2 present the weight after each cycle (mg), and A presents the total surface area of the sample (cm^2).

In case of wt. % Na_2SO_4-25K_2SO_4 molten salt medium, weight gain were observed in all samples at the first 12 hours of the corrosion process. Especially, after the first cycle, a large weight gain (21 mg/cm^2) was recorded in the Ti-48Al. It suggests that the corrosion process is controlled by the formation of corrosion products at this stage. Subsequently, the weight losses of studied samples increase with increasing the exposure time, indicating that the corrosion products are volatile or spall off. The Ti-48Al-2Mn and Ti-48Al-2Mn-2Mo samples experienced similar corrosion behavior resulting in the weight change of 2.4 and 2.7 mg/cm^2 until 48 h, respectively. After 48 h of exposure, Ti-48Al-2Mn-2Mo showed weight loss until 84th hours and then slightly gains weight, while Ti-48Al-2Mn showed positive weight changes until 144th hours followed by weight loss until the end of the corrosion experiment. After 108 h of exposure, Ti-48Al-2Cr and Ti-48Al-2Cr-2Mo samples have nearly similar corrosion kinetics and their final weight changes were about -6.3 and -13.5 mg/cm^2, respectively.

Figure 4

As far as the wt. % Na_2SO_4-25NaCl salt mixture is concerned, the highest weight losses occurred in the samples when NaCl was introduced into the medium. Thus, the weight change rate of Ti-48Al was -10.5 mg/cm^2 in the medium without NaCl, while its weight change rate was -33.4 mg/cm^2 in the medium with NaCl. This means that sodium chloride is much more corrosive than potassium sulfate. The weight changes of the Ti-48Al, Ti-48Al-2Cr and Ti-48Al-2Mn samples increased slowly at first and then gradually decreased at the end of the hot corrosion process. As for the Ti-48Al-2Cr-2Mo and Ti-48Al-2Mn-2Mo, the samples consistently showed weight loss up to 180 hours without an evident initiation stage. The Mo-added samples behaved similarly in terms of corrosion resistance, but Ti-48Al-2Cr-2Mo lost more weight during the later stage, indicating that the Mn was a more beneficial ternary element compared to Cr. After 180 h of exposure, overall weight changes of the Ti-48Al-2Mn-2Mo and Ti-48Al-2Cr-2Mo were about -43 and -54 mg/cm^2, respectively. It is important to mention that Mo-added samples experienced more weight loss compared to the other samples in both molten salt mixture. The specific reasons for the weight loss in Mo-added samples will be explained in the discussion section. In a word, by considering the obtained data in Fig. 4, the hot corrosion resistance of RS-processed Ti-48Al based intermetallics in both molten salt mixtures decreases in this order: Ti-48Al-2Mn>Ti-48Al-2Cr>Ti-48Al>Ti-48Al-2Mn-2Mo>Ti-48Al-2Cr-2Mo.

3.3. Phase composition of hot corrosion products

X-ray diffraction (XRD) analyses were performed to identify the corrosion products formed on the samples after hot corrosion for 180 hours. The surface XRD analysis results of the hot corroded samples are shown in Figure 5. It is considered that the phase composition of corrosion products formed on the surface was affected by temperature and salt chemistry. For the samples in the mixture of wt. % Na_2SO_4-25K_2SO_4 molten salt, the identified corrosion products were TiO_2, Al_2O_3 and $Na_2Ti_3O_7$ after hot corrosion at 900°C for 180 h (Fig. 5a). It can be clearly discerned that the weak diffraction signals corresponding the TiAl and Ti_3Al phases were also found in the XRD analyes. It is considered that the mentioned matrix phases detected due to the exfoliation of the corrosion products.

Figure 5

When the samples were exposed to the mixture of wt. % Na_2SO_4-25NaCl molten salt at 800°C for 180 h, as can be seen from Fig. 5b, the corrosion products were $Na_2Ti_9O_{19}$, $Na_4Ti_5O_{12}$, TiO, TiO_2 and Al_2O_3. Besides, diffraction peaks with lower intensity from NaCl phase were also observed in the XRD analysis results, showing that a minor amount of residual existed on the corrosion scale. According to the obtained XRD results, it can be said that the presence of sodium-titanium oxides can be occurred by the reactions between TiO_2 and molten salts. This is consistent with the results reported by Lin et al. [14].

3.4. SEM/EDS analysis of hot corroded samples

3.4.1. Characterization of surface microstructure

The SEM images displaying the surface morphologies of the samples after corrosion in wt. % Na_2SO_4-25K_2SO_4 molten salts at 900°C for 180 hours are presented in Fig. 6. Table 4 is the corresponding chemical composition of the surface analyzed by EDS. It was observed in Figure 6 that spallation occurred on the scales of the tested samples. The corrosion scale of the Ti-48Al was porous and also a big crack was observed on the edge of the scale. A higher magnification of SEM image of the internal surface showed that the scale consisted of a flat area with dark tones and gray crystals (spots 1 and 2 in Fig. 6). Chemical analysis by EDS indicated that the flat area has composition corresponding to the alumina-rich and the crystals consisted of titanium oxides. The titanium oxide grains formed on the surface have a polyhedral structure. SEM images of the Ti-48Al-2Cr sample show the spherical shaped craters covered with sharp-edged and round-shaped crystals in some places. The enlarged SEM image of the scale on the surface reveals that the scale was made up of a dark grey region (area 3 in Fig. 6) and a light grey region (spot 4 in Fig. 6). The obtained XRD and EDS

analysis results indicated that the compositions of dark grey and light grey regions corresponded to Al_2O_3 and TiO_2 phases, respectively. The scale formed on the hot corroded Ti-48Al-2Mn sample spalled off, as shown in Fig. 6. EDS analysis revealed that the internal and external surfaces have almost similar chemical compositions. However, the higher concentration of sodium was found in the external surface compared with the internal surface, as shown in Table 4. By considering the combination of the XRD and EDS analyses, the scale consisted of TiO_2, Al_2O_3 and $Na_2Ti_3O_7$ phases. The enlarged SEM images of the internal surface showed titanium oxide grains with a typical pillar-like structure. As far as samples with Mo addition are concerned, the similar surface morphology was observed in both samples. Bumpy surfaces and deep pits are clearly visible in the scales SEM image of the spalled area in the Ti-48Al-2Mn-2Mo sample shows that the oxides of TiO_2, Al_2O_3 and $Na_2Ti_3O_7$ phases are discontinuous.

The Ti-48Al-2Cr-2Mo sample covered with smaller round shaped oxide crystals (area 9 in Fig. 6) as compared to the Ti-48Al-2Mn-2Mo sample. EDS analysis shows that the dark region (area 9 in Fig. 6) has a higher content of Na, while the bright region (area 10 in Fig. 6) has a higher content of Al. It is important to note that the molybdenum could hardly be found due to the fact that MoO_3 could be volatilized above 700°C [34], as presented in Table 4. It can be inferred that the pores caused by volatile MoO_3 may play a significant role in the inward diffusion of the molten salt. Therefore, the Mo-added samples undergo severe degradation in the presence of molten salts.

Figure 6

Table 4

Fig. 7 illustrates the surface morphology of the studied samples after hot corrosion in the wt. % Na_2SO_4-25NaCl molten salt at 800°C for 180 h and Table 5 corresponds to the EDS analysis results. Surface morphologies of the samples were rather different from those of the samples in K_2SO_4-containing salt mixture. The Ti-48Al sample had a porous scale and many small pits were found on the surface (Fig. 7). XRD and EDS results (Figure 5b and Table 5) showed that the scale formed on the surface was composed of titanium oxides, Na-Ti oxides and alumina. The surface is covered with corrosion products, which seem mud-like at a higher magnification, with elevated contents of sodium. SEM surface image of the Ti-48Al-2Cr sample shows that the scale was peeled off from the surface (Fig. 7). It is worth noting that the large amounts of corrosion products are stacked in layers, resulting in a bumpy surface morphology. The detailed SEM image of area 4 displays that the surface is mostly covered by

equiaxed oxide grains with polyhedron-shape. According to the EDS analyses, the equiaxed oxide grains have a composition of 28.3Ti-3.9Al-0.1Cr-64.8O-2.4Na-0.2Cl-0.3S (at.%). and Fig. 5b reveals that they are TiO_2 phase. SEM image in Fig. 7 shows that the fine rod-like shaped crystals covered with a relatively smooth layer are found on the Ti-48Al-2Mn sample. At the same time, some cracks were observed on the surface. The EDS analyses indicate that the scale mainly contains Ti, O, Na, Cl and a minor amount of Al. It can be seen that the severe spallation of corrosion products formed on the Ti-48Al-2Mn-2Mo sample occurred after exposure to the wt. % Na_2SO_4-25NaCl deposits for 180 h at 800°C. The enlarged SEM image of the spalled area in Fig. 7 showed that the surface of the sample was porous and rough and there were also several pits. As for the Ti-48Al-2Cr-2Mo sample, the presence of large cracks was observed on the scale of the sample. Internal surface (area 10 in Fig. 7) has a relatively smooth surface, while the external surface (area 11 in Fig. 7) has an undulating morphology. It can be considered that excessive weight loss in Mo-added samples (Fig. 4b) is a sign of the spallation of corrosion products and the formation of cracks.

Figure 7

Figure 7 Continued

Table 5

3.4.2. Cross-sectional analysis

Together with weight change measurement, detection of corrosion products and observation of surface morphology, the examination of corrosion degradation rate was also performed by cross-sectional analysis. The cross-section SEM images of the TiAl based samples after hot corrosion in the mixture of Na_2SO_4 and K_2SO_4 melts for 180 h at 900°C can be seen in Fig. 8. By considering the results of EDS analysis in Table 6, titanium, aluminum, oxygen and a minor amount of sodium are the main components of the corrosion products. The cross-sectional microstructures of the samples show that the corrosion scales are mainly composed of light gray and a mixture of light gray and dark gray. The composition of external layers (spots 1, 4, 7, 10 and 13 in Fig. 8) corresponded to titanium-rich oxides. Beneath this layer, the Ti and Al rich oxide layers (areas 2, 6, 8, 11 and 14 in Fig. 8) happen alternately. EDS analysis reveals that these oxides are TiO_2, Al_2O_3 and $Na_2Ti_3O_7$, which is consistent with the XRD analyses in Fig. 5a. Figure 8 shows that the scales formed on the samples were porous and loosely adherent to the substrates. In addition, many pits and micro cracks were found in

the scales of all samples. However, it was observed that a crack parallel to the surface in the scale of Ti-48Al. It is important to highlight that oxygen and molten salt mixture can diffuse to the substrate due to the fact that the samples have a porous structure. Presence of oxygen (spots 3, 9, 12 and 15 in Fig. 8) is an indication of internal oxidation occurred in the substrate and along the grain boundaries. The hot corrosion attack through the grain boundaries are more than the interior of the grains, indicating that the grain boundaries are more susceptible. It can be clearly noticed that the Ti-48Al sample undergoes more severe internal oxidation compared to other samples. At the location close to the substrate (spot 5 in Fig. 8), there was a bright phase consisting of an aluminum-depleted area. According to Ti-Al binary phase diagram, the composition of mentioned area corresponds to an α_2-Ti_3Al phase (at.% Al 22-39). The Ti_3Al phase is confirmed by XRD analysis in Fig. 5a.

Figure 8
Table 6

The cross-section SEM images of the TiAl based samples after hot corrosion in the mixture of Na_2SO_4 and NaCl melts for 180 h at 800°C are shown in Fig. 9. It is worth noting that the cross-sectional microstructures of the samples are different from the ones in the case of K_2SO_4-containing deposit. As can be seen from Fig. 9, large cracks were observed on the scale of all samples regardless of alloy composition. In particular, the corrosion scales formed on the Ti-48Al-2Cr, Ti-48Al-2Mn and Ti-48Al-2Mn-2Mo samples tend to part off the substrate. It is considered that the cyclic test plays a key role to generate cracks due to the rapid-changing temperature during the cycle. From the EDS analysis listed in Table 7, the external layer (Spot 1 in Fig. 9) of the scale formed on the Ti-48Al is found to be TiO_2 phase. Interestingly, this TiO_2 layer featured a uniform structure such as a coating layer. However, many cracks parallel to the surface are found beneath this layer. Spots 4, 9, 15 and 20 indicate the presence of major amount of oxygen, titanium and sodium along with small amount of aluminium and chlorine thereby suggesting the possibility of formation of sodium-titanium oxides. XRD analysis results in Fig. 5a revealed that these corrosion products are composed of $Na_2Ti_9O_{19}$ and $Na_4Ti_5O_{12}$. The chemical composition of the spots 5, 10, 16 and 21 which lie on the beneath of the outer layer corresponded to titanium-rich oxides. By considering the EDS analysis (Table 7) in combination with XRD results (Fig. 5a), it is reasonable to infer that it is TiO_2 phase. A bright phase (spot 12 in Fig. 9) with a relatively higher amount of sodium and chlorine could be seen in the scale. Spots 6, 13, 17 and 22 show the presence of major amount of oxygen and aluminium along with minor amount of titanium, sodium and

chlorine. The obtained EDS results indicate the formation of alumina, which is consistent with the XRD analysis in Fig. 5a.

Figure 9

Spots 7 and 18 which lie on the crack show the presence of an elevated amount of oxygen (at.% 50.4 and 42.9, respectively), while the spots 8 and 19 which lie on the beneath the crack show the presence of a smaller amount of oxygen (at.% 4.4 and 10.6, respectively). This indicates that the crack prevents further diffusion of oxygen into the substrate.

Table 7

4. Discussion

In conventional powder sintering, the sample is usually heated by a furnace. In order to obtain a uniform temperature distribution and microstructural homogeneity, slow heating rates and long sintering cycles (several hours, even days) are mostly required [35]. In contrast, since an intense electric current flows directly through the compact during RS process, the heat is produced within the sample and as a result, very rapid heating rates achieve. Regarding the main drawbacks of the RS process, they include the difficulty of achieving a uniform heat distribution inside the compact during operation and the absence of sufficient theoretical knowledge of the existence of various mechanisms [36]. However, much of the discussion on electric current assisted manufacturing methods has focused on the enhancement in the densification of materials. As an example of the effect of current in densification, Densification experiments by means of spark plasma sintering (SPS) and hot pressing (HP) have been performed to make a comparison of the densification kinetics of TiAl. Experiments revealed that the SPS and HP kinetics exhibit no significant differences [37].

It is possible to compare the microstructure of alloys produced by RS with that produced by other sintering techniques. For example, one method similar to RS can be SPS. Lagos and Agote [38] sintered Ti-48Al-2Cr-2Nb alloy by using SPS, and it was observed that the microstructure obtained by RS (Fig. 3) and by SPS are similar. However, the RS technology, whose cost is lower than spark plasma sintering (SPS), is a viable alternative for producing TiAl based intermetallics. In another example, Ti-36Al (wt.%) alloy was sintered using the hot pressing method for two hours at 1300°C and it was reported that the microstructure of the alloy consists of TiAl phase [39]. Accordingly, the sintering time of the RS process was 35 min (in this study) and for HP was 120 min. The saving of processing time mainly relates to a shortening of the dwell from 120 to 35 min.

Sodium sulfate and sodium chloride are the main components of salt deposits used to determine the hot corrosion rates of materials. The results obtained the used scenario in this study show that the chemical composition of salt deposits has a significant influence on the hot corrosion resistance of investigated samples. This observation also is in good agreement with the one reported by other authors for varied compositions of TiAl [17-19]. Godlewska et al. [40] studied the corrosion behavior of (at.%) Ti-46Al-8Ta alloy contaminated with NaCl, Na_2SO_4 and Na_2SO_4-NaCl deposits at 700 and 800°C, they found the salt deposits have a detrimental effect on the corrosion behavior of the alloy. In order to demonstrate the extent of degradation of samples in the salt mixtures, macrophotos of the samples were taken after hot corrosion tests (Figs. 10 and 11). It is important to note that the NaCl-containing salt mixture significantly accelerates the degradation of the samples. It is reasonable to conclude that the composition of the salt is a significant parameter when considering material damage during hot corrosion. According to many authors, the NaCl behaves much greater corrosive in hot corrosion tests in comparison with Na_2SO_4 and K_2SO_4 substances [19,40-43]. When the weight changes in samples exposed to both corrosive medium were compared, the NaCl-containing medium caused the most weight loss (Fig. 4a,b) and severe scale spallation (Figs. 10 and 11). This means that the scales formed in the samples cannot protect the matrix and the matrix is exposed to further corrosion attacks. When considering the cross-sectional images of the samples (Figs. 8 and 9), it is important to note that the corrosion scales formed on all samples in the mixture of wt. % Na_2SO_4-25NaCl salt are quite thicker than in the experiment with the mixture of wt. % Na_2SO_4-25K_2SO_4 salt. For example, the thickness of the scale on Ti-48Al sample in a mixture of wt. % Na_2SO_4-25NaCl salt was about 634 μm, whereas in a mixture of wt. % Na_2SO_4-25K_2SO_4 salt, the scale on the sample was about 125 μm thick. It follows from the comparison of the obtained results (visual inspection, weight change curves, examination of cross-sectional and surface morphologies of samples) that NaCl was the substance which increased brittleness, weight loss, cracks formation and spallation of corrosion product. As mentioned in the examination of the cross-sectional microstructure, the scales on the corroded samples were cracked in the direction parallel to the interface.

Figure 10

Figure 11

The cause for the crack formation can be ascribed to the stress generated from the fast growth of scale. During hot corrosion, a molten salt film covers the sample and complex stresses can be formed in the film such as the thermal stress and growth stress. The presence of cracks

provided evidence that the internal stresses are bigger than the strength of the scale. Therefore, the corrosion attack proceeds rapidly with the increase in exposure time [44].

When the corrosion behavior of the samples is evaluated in terms of alloy composition, as can be seen in Fig. 10, in Na_2SO_4-K_2SO_4 molten salt, the silver metallic color of the Ti-48Al sample turns into the surface which was composed of green, white and dark gray. The corrosion products were severely spalled when the sample was touched for cleaning, which showed their brittleness and poor adherence to the substrate. After 180 h of hot corrosion at 900°C, the corrosion scales on Ti-48Al-2Cr and Ti-48Al-2Mn samples were relatively dense with dark yellow and brown, respectively. This means that the type of corrosion products could change. It is worth noting that both mentioned samples exhibited better corrosion resistance compared with the Ti-48Al. Therefore, Cr and Mn alloying elements have a beneficial effect on hot corrosion properties of samples. This evidence is in good agreement with the one reported by Leyens et al. [45] who investigated corrosion behavior of NiAl added with various elements in Na_2SO_4 salt at 950°C and observed that only Cr (at.% 2) improved hot corrosion resistance. These authors attributed the role of chromium to maintaining salt basicity in a range where Al_2O_3 solubility is minimal. In the case of Mo-added samples corroded in Na_2SO_4-K_2SO_4 molten salt, deep pits can be seen on the surface of samples (Fig. 11). Such pits caused a significant weight loss in the samples, as shown in Fig. 4a. A noteworthy fact is that the corrosion mechanism is more complex in the Mo-added samples.

Alloys containing refractory components such as W, Mo and V may be subjected to severe acidity dissolution reactions because the oxides of these elements react with molten sulphate and by reducing the oxide ion activity of the melt, the conditions for acidic dissolution of the corrosion products are provided [46]. This type of hot corrosion is called alloy-induced acidic fluxing, and [4,47], unlike basic dissolution, it is a self-sustaining process [29]. Therefore, only one application of salt layer may cause complete degradation of the sample. Acidic conditions in the Na_2SO_4 molten salt may be formed by the incorporation of MoO_3 and thus Al_2O_3 and TiO_2 undergo alloy-induced acidic fluxing shown in the following reaction:

$$Al_2O_3 + 3MoO_3 \text{ (in } Na_2SO_4) = 2Al^{3+} + 3MoO_4^{2-} \quad (5)$$

$$TiO_2 + 2MoO_3 \text{ (in } Na_2SO_4) = Ti^{4+} + 2MoO_4^{2-} \quad (6)$$

Furthermore, by reacting with MoO_3, Na_2SO_4, the O^{-2} ion activity of the liquid solution is reduced and the basic dissolution mechanism is prevented [4]. The reaction can be expressed by the following equation,

$$MoO_3 + Na_2SO_4 = Na_2MoO_4 + SO_{3(g)} \quad (7)$$

Because of the active gradient, the MoO_4^{2-}, Ti^{4+} and Al^{3+} ions diffuse through the molten salt to the molten/gas interface. The MoO_4^{2-} ion can evaporate as the form of corresponding oxides because of high vapor pressure, thus can liberate oxygen ions. The increasing oxygen ions will cause high oxygen activity at the molten/gas interface [46]. Thus, a negative solubility gradient is established between the oxide/molten interface and the molten/gas interface. The TiO_2 and Al_2O_3 corrosion products re-precipitate to the melt/gas interface have porous and non-protective features. It should be noted that this type of acidic dissolution is self-sustaining because MoO_3 can be produced continuously at the alloy/molten interface and evaporate at the molten/gas interface [4]. The attack initiates on local sites with Mo-rich on the substrate (spots 5 and 10 in Fig. 3) because the activity of MoO_3 in the molten sulfate is higher in these regions. The deep pits, seen in the macro photos of Mo-added samples (Fig. 10) are the evidence of alloy-induced acidic fluxing. This form of attack takes place till Mo component of the alloy is completely consumed. Moreover, it can be considered that greater weight loss exhibited by the Mo-added samples due to the alloy-induced acidic fluxing (Fig. 4a). Goebel et al. [48] studied the hot corrosion properties of Mo, W and V added-NiAl and NiAlCr alloys in Na_2SO_4 salt at 1000°C and observed that all their alloys were subjected to severe corrosion attack. Besides, the mentioned alloying elements were detected to be accumulated at the substrate/scale interface and these regions pioneered the initiation of corrosion attack.

On the other hand, the melting point of Na_2MoO_4 formed as a result of Eq. 7 is 687°C and thus plays a significant role in the melting temperature of that molten salt. A lower temperature for the hot corrosion process indicates that the temperature range for the attack is carried to lower temperatures. However, faster degradation of Mo-added samples not only attributed to the formation of Na_2MoO_4, but also contributed to the degradation of the MoO_3 with a melting point of 795°C.

It is considered that the activities of SO_3 and Na_2O are related through the Na_2SO_4 dissociation equilibrium. This reaction is shown below in Eq. 8 [4,6,40,41].

$$Na_2SO_4 = Na_2O + SO_3 \text{ or } Na_2SO_4 = Na_2O + SO_2 + \tfrac{1}{2} O_2 \quad (8)$$

As can be seen in the Na-S-O phase stability diagram (Fig. 12), the composition of Na_2SO_4 changes due to the dissociation [29]. The composition of Na_2SO_4 at a certain temperature is determined by the Po_2 and by either a_{Na_2O} or Pso_3. Since the formation and consumption of O^{2-} can change the composition of the salt, it may become more acidic (higher SO_3 activity) or more basic (higher Na_2O activity).

Figure 12

The activity of either SO_3 or Na_2O plays a significant role in the dissolution of oxides formed on surface. As the activity of Na_2O (a_{Na_2O}) is higher at high temperatures reacts with (Na_2O) TiO_2 and Al_2O_3 as following equations:

$$3TiO_2 + Na_2O = Na_2Ti_3O_7 \quad (9)$$

$$Al_2O_3 + Na_2O = 2NaAlO_2 \quad (10)$$

The thermodynamic calculations show that the equations (9) and (10) can be occurred due to their Gibbs free energies (ΔG^o) are negative (Table 8). $Na_2Ti_3O_7$ phase is found in EDS analysis results (Fig. 5a) and this indicates that the equation (9) realized. However, since $NaAlO_2$ is water soluble [42], the sample may have been removed during the cleaning process. In addition, the S, released by the $SO_3 = S_2 + 3O_2$ reaction, diffuses to the substrate by reacting with the components of the alloy to form the sulfides through cracks and pores on the surfaces of the samples (Figs. 6 and 7). However, aluminium or titanium sulphides were not found in the XRD patterns. It was reported that sulphide compounds are usually unstable in air. Therefore, when they are subjected to oxidation, they form the corresponding oxides and release sulphur simultaneously via Eq. (11) [41]. Released S diffuses again inward to substrate to expose the samples to sulfidation.

$$2MS_x + yO_2 = 2MO_y + 2xS \quad (11)$$

As a result of basic dissolution of an oxide, a complex anion can be formed, or as a result of its acidic dissolution, it can correspond into anions and cations. The acid-base mechanism for Al_2O_3 and TiO_2 is given as [6]:

$$Al_2O_3 + O^{2-} = 2AlO_2^{2-} \quad \text{(basic dissolution)} \quad (12)$$

$$Al_2O_3 = 2Al^{3+} + 3O^{2-} \quad \text{(acidic dissolution)} \quad (13)$$

$$Ti^{4+} + 2O^{2-} = TiO_2^{2-} \quad \text{(basic dissolution)} \quad (14)$$

$TiO_2 = Ti^{4+} + 2O^{2-}$ (acidic dissolution) (15)

As a result of the equations 12 and 14, the oxygen ion activity in the salt is reduced and this causes a driving force for the acidic dissolution to occur. Since the negative solubility gradient is established in the molten salt, generated ions will diffuse from the interface of oxide/molten salt to the interface of molten salt/gas where solubility is lower, and the ions will precipitate out of solution. The precipitated oxides are loose or porous and will give no protection against corrosion.

Many studies are in agreement that sodium chloride can interact with oxygen to destabilize several oxides (such as Al_2O_3, Cr_2O_3, Ta_2O_5, Nb_2O_5) [40,41,47,49]. The following reactions can be given for sodium aluminate and sodium titanate :

$4NaCl_{(k)} + 2Al_2O_{3(k)} + O_{2(g)} = 4NaAlO_{2(k)} + 2Cl_{2(g)}$ (16)

$2NaCl_{(g)} + 9TiO_{2(k)} + ½\ O_{2(g)} = Na_2Ti_9O_{19(k)} + Cl_{2(g)}$ (17)

$4NaCl_{(g)} + 5TiO_{2(k)} + O_{2(g)} = Na_4Ti_5O_{12(k)} + 2Cl_{2(g)}$ (18)

The above thermodynamic predictions are consistent with XRD analysis results (Fig. 5b). The released Cl_2 from the above reactions (Eqs. 16-18) can diffuse by pores, cracks as well as grain boundaries into the substrate and react with alloying elements to generate volatile chlorides such as $TiCl_4$ and $AlCl_3$ [40,42,50] :

$1/2Ti + Cl_{2(g)} = 1/2TiCl_{4(g)}$ (19)

$2/3Al + Cl_{2(g)} = 2/3AlCl_{3(g)}$ (20)

The ΔG values for almost all reactions listed in Table 8 are negative, which indicates that they might be taken place on the basis of thermodynamics. By considering the thermodynamic calculations, the most probable in Table 8 chloride species is $AlCl_3$ due to the most negative ΔG value. These formed chloride species are volatile and may diffuse towards the outer surface with high oxygen potential and, as thermodynamically lesser stable than the corresponding oxides, they may oxidize in the following manner :

$TiCl_{4(g)} + O_{2(g)} = TiO_2 + 2Cl_{2(g)}$ (21)

$4/3AlCl_{3(g)} + O_{2(g)} = 2/3Al_2O_3 + 2Cl_{2(g)}$ (22)

The Cl_2 is generated again resulting from the above reactions (Eqs. 21 and 22) and may again react with alloy components as in Eqs. 19 and 20. Thus the above process will occur cyclically and chloride will continue to be active in the chlorination/oxidation of the samples.

For the experimental conditions applied in this study, Cl_2 can be recognized to play an active role in accelerating the degradation process of the sample. This proposition can be confirmed in considering that the more degradation of the samples in the presence of NaCl-containing medium (Figs. 7, 9 and 11). Besides, the presence of this mechanism is experimentally further evidenced by the detection of chlorides at the substrate/corrosion scale interface (spots 2, 3, 7, 11, 12, 18, 19 and 24 in Fig. 9). It is important to highlight that the melting points of $TiCl_4$, $AlCl_3$ and $MoCl_4$ are -25°C, 193°C and 317°C, respectively. Moreover, as can be seen in Fig. 13, these chlorides have high vapor pressures. Therefore, the volatilization of these chlorides can provide a channel for the diffusion of ions species and molten salts, and also makes corrosion scale porous. As the corrosion proceeds, it generates the cracks between substrate and scale (Fig. 9). Many studies have reported that [41,42,51,52] the main reason for spallation and cracking of the scale is the formation of gaseous species, which is also confirmed by the findings of this study.

It should be noted that the composition of salt mixture (wt. % Na_2SO_4-25NaCl) used in this study close to the eutectic composition (wt. % 69.1 NaCl at 628°C) in the NaCl-Na_2SO_4 system [29]. This may be another reason why samples experience more severe attacks.

Table 8

Figure 13

It has been reported that a direct comparison of the hot corrosion behavior of the alloys cannot be made due to different experimental conditions [42]. However, when comparing the hot corrosion behavior of TiAl alloys in this study with TiAl alloys in another study, the differences that should occur should be attributed not only to the corrosion test procedure, but also to other factors such as the manufacturing process and alloy composition. For example, Zhang et al. [50] investigated the corrosion behavior of a high Nb-containing TiAl alloy (at.% Ti-45Al-8.5Nb-0.2W-0.2B-0.02Y) in wt.% Na_2SO_4-25 NaCl salt mixture for 50 h at 800°C. After hot corrosion for 50 h, they found that the weight change of TiAl alloy was - 7.50 mg/cm^2. In this study, the weight changes of the alloys (Ti-48Al, Ti-48Al-2Cr, Ti-48Al-2Mn, Ti-48Al-2Mn-2Mo and Ti-48Al-2Cr-2Mo) exposed to the same corrosion medium at 900°C were 0.2, -5.1, 13.5, -10.9 and -25.8, respectively. The main reason for this difference in the corrosion resistance of alloys can be attributed to alloy composition and exposure temperature, but we also think that the production method used is an important factor. It can be seen from Table 2 that the alloys produced by RS have a porosity of 1.26 to 3.30%. These porosities in alloys play an important role in the inward movement of diffusion species

involved in the corrosion process. Moreover, the pores can be caused localized corrosion as they have high free energy, and as a result, a large material loss occurs. The electric current flowing through the powders during RS enhances the sintering kinetics and it decreases the sintering time and temperature compared to the conventional methods. However, since a paper investigating the hot corrosion behavior of TiAl produced with conventional sintering methods cannot be found in the open literature, the effect of the applied electric current on the corrosion behavior could not be emphasized. Obviously, to clarify the corrosion mechanism of electric field/current-assisted sintering, a comparative study on RS and other techniques (such as pressureless sintering, hot pressing) is necessary.

As a final note, it has been reported [42] that the TiAl alloys have poor corrosion resistance in corrosive molten salts (Na_2SO_4 or NaCl). Based on our knowledge, the hot corrosion behaviors of materials can be affected by the testing procedures. In laboratory studies, several testing methods can be preferred to estimate corrosion kinetics of samples, such as spraying of salt solutions, immersion in molten salt and deposition from vapour phase. As stated in the experimental section of this study, the samples were immersed in the molten salt mixture. The salt amount used in this study is quite larger than that of deposited on aero gas turbine while in service conditions (about 0.27 $\mu g/cm^2$ h) [42]. Thus, it can be expected that the samples experienced severe degradation after 180 h of exposure.

5. Conclusions

In this study, resistance sintering (RS) technology was effectively applied for production of TiAl based intermetallics added Cr, Mn and Mo alloying elements and the influence of these additions on the hot corrosion behavior of alloys in the molten salt environment consisting of % wt. Na_2SO_4-25K_2SO_4 and Na_2SO_4-25NaCl was explored. The following main conclusions can be drawn from this study:

1. TiAl based intermetallics prepared by RS consisted of γ-TiAl and α_2-Ti_3Al phases.

2. The weight losses of Mo-added samples are more than those of Mo-free samples in both corrosive salt medium due to the alloy-induced acidic dissolve. However, the corrosion bahavior of samples not only affected on the Mo additions but also on NaCl-containing corrosive medium.

3. The corrosion resistance of Ti-48Al-2Cr and Ti-48Al-2Mn was better compared to other samples. It can be said that Cr and Mn additions improved the hot corrosion resistance of investigated samples in this study.

4. The salt compositions used in this study allowed to demonstrate the effect of the samples on the hot corrosion behavior. In the case of Na_2SO_4-25NaCl salt mixture, the scales formed on samples were cracked in the direction parallel to the surface. The formed scales on corroded samples were thicker, more porous and loose. In addition, severe spallation of corrosion products has occurred.

5. During the hot corrosion process, NaCl played a crucial role in initiating the severe corrosion attacks due to the chlorination/oxidation cyclic reactions.

Data availability

The raw/processed data required to reproduce these findings cannot be shared at this time due to technical or time limitations.

Author statement

Y. Garip: Main contributor, original draft preparation, Data curation, Experiment participator, Conceptualization, Writing- Reviewing and Editing

O. Ozdemir: Supervision, Validation, Conceptualization

Declaration of interests

The authors declare that they have no known competing financial interests or personal relationships that could have appeared to influence the work reported in this paper.

References

[1] J. M. Alvarado-Orozco, J. E. Garcia-Herrera, B. Gleeson, F. S. Pettit, G. H. Meier, Reinterpretation of Type II Hot Corrosion of Co-Base Alloys Incorporating Synergistic Fluxing, Oxid. Met. 90 (2018) 527-553. https://doi.org/10.1007/s11085-018-9853-6.

[2] D. A. Shifler, Hot corrosion: a modification of reactants causing degradation, Mater. High. Temp. 35 (2018) 225-235. https://doi.org/10.1080/09603409.2017.1404692.

[3] I. Gurrappa, Mechanism of Degradation of Titanium Alloy IMI 834 and its Protection under Hot Corrosion Conditions, Oxid. Met. 59 (2002) 321-332. https://doi.org/10.1023/A:1023044111767.

[4] B. S. Lutz, J. M. Alvarado-Orozco, L. Garcia-Fresnillo, G. H. Meier, Na_2SO_4-Deposit Induced Corrosion of Mo-Containing Alloys, Oxid. Met. 88 (2017) 599-620. https://doi.org/10.1007/s11085-017-9746-0.

[5] Q. Jia, D. Li, S. Guan, Z. Zhang, N. Zhang, W. Zhao, Oxidation Resistance and Modification Reaction Mechanism of Al Coating Sprayed on Pure Ti Substrate, Adv. Mater. Sci. Eng. (2018) 1-9. https://doi.org/10.1155/2018/1403521.

[6] Y. Garip, O. Ozdemir, Comparative study of the oxidation and hot corrosion behaviors of TiAl-Cr intermetallic alloy produced by electric current activated sintering, J. Alloy Compd. 780 (2019) 364-377. https://doi.org/10.1016/j.jallcom.2018.11.324.

[7] Y. Garip, O. Ozdemir, Hot corrosion behavior of Ti-48Al and Ti-48Al-2Cr intermetallic alloys produced by electric current activated sintering, Metall. Mater. Trans. A 49A (2018) 2455-2462. https://doi.org/10.1007/s11661-018-4581-8.

[8] M. Bik, A. Gil, M. Stygar, J. Dąbrowa, P. Jeleń, E. Długoń, M. Leśniak, M. Sitarz, Studies on the oxidation resistance of SiOC glasses coated TiAl alloy, Intermetallics 105 (2019) 29-38. https://doi.org/10.1016/j.intermet.2018.09.014.

[9] H. Chen, X. Li, Z. Chen, R. Zhang, X. Ma, F. Zheng, Z. Ma, F. Pan, X. Lin, Investigation on electronic structures and mechanical properties of Nb-doped $TiAl_2$ intermetallic compound, J. Alloy Compd. 780 (2019) 41-48. https://doi.org/10.1016/j.jallcom.2018.11.362.

[10] Y. Jianga, Y. Hea, C.T. Liu, Review of porous intermetallic compounds by reactive synthesis of elemental powders, Intermetallics 93 (2018) 217-226. http://dx.doi.org/10.1016/j.intermet.2017.06.003.

[11] R. Swadźbaa, L. Swadźba, B. Mendala, B. Witala, J. Tracz, K. Marugi, Ł. Pyclik, Characterization of Si-aluminide coating and oxide scale microstructure formed on γ-TiAl alloy during long-term oxidation at 950°C, Intermetallics 87 (2017) 81-89. http://dx.doi.org/10.1016/j.intermet.2017.04.015.

[12] M. P. Brady, W. J. Brindley, J. L. Smialek, I. E. Locci, The Oxidation and Protection of Gamma Titanium Aluminides, JOM 48 (1996) 46-50. https://doi.org/10.1007/BF03223244.

[13] E. A. Loria, Gamma titanium aluminides as prospective structural materials, Intermetallics 8 (2000) 1339-1345. https://doi.org/10.1016/S0966-9795(00)00073-X.

[14] Z. Lin, Y. Zhou, M. Li, J. Wang, Hot corrosion and protection of Ti_2AlC against Na_2SO_4 salt in air, J. Eur. Ceram. Soc. 26 (2006) 3871-3879. https://doi.org/10.1016/j.jeurceramsoc.2005.12.004.

[15] V. Mannava, A. SambasivaRao, M. Kamaraj, R. S. Kottada, Influence of Two Different Salt Mixture Combinations of Na_2SO_4-NaCl-$NaVO_3$ on Hot Corrosion Behavior of Ni-Base Superalloy Nimonic263 at 800°C, JMEPEG 28 (2019) 1077-1093. https://doi.org/10.1007/s11665-019-3866-4.

[16] I. Gurrappa, I.V.S. Yashwanth, I. Mounika, H. Murakami, S. Kuroda, The Importance of Hot Corrosion and Its Effective Prevention for Enhanced Efficiency of Gas Turbines, Gas Turbines-Materials, Modeling and Performance (2015) 55-102. http://dx.doi.org/10.5772/59124.

[17] Z. Tang, F. Wang, W. Wu, Hot-corrosion behavior of TiAl-base intermetallics in molten salts, Oxid. Met. 51 (1999) 235-250. https://doi.org/10.1023/a:1018818622547.

[18] K. Zhang, Z. Li, W. Gao, Hot corrosion behaviour of Ti-Al based intermetallics, Mater. Lett. 57 (2002) 834-843. https://doi.org/10.1016/s0167-577x(02)00882-0.

[19] Z. Yao, M. Marek, NaCl-induced hot corrosion of a titanium aluminide alloy, Mater. Sci. Eng. A 192-193 (1995) 994-1000. https://doi.org/10.1016/0921-5093(95)03345-9.

[20] S. Shu, F. Qiu, B. Xing, S. Jin, J. Wang, Q. Jiang, Effect of strain rate on the compression behavior of TiAl and TiAl-2Mn alloys fabricated by combustion synthesis and

hot press consolidation, Intermetallics, 43 (2013) 24-28. https://doi.org/10.1016/j.intermet.2013.07.003.

[21] A. Duarte, F. Viana, H.M.C.M. Santos, As-cast titanium aluminides microstructure modification, Mater. Res. 2 (1999) 191-195. http://dx.doi.org/10.1590/S1516-14391999000300013.

[22] L. Yang, L.H. Chai, Y.F. Liang, Y.W. Zhang, C.L. Bao, S.B. Liu, J.P. Lin, Numerical simulation and experimental verification of gravity and centrifugal investment casting low pressure turbine blades for high Nb-TiAl alloy, Intermetallics 66 (2015) 149-155. http://dx.doi.org/10.1016/j.intermet.2015.07.006.

[23] M.N. Mathabathe, A.S. Bolokang, G. Govender, C.W. Siyasiya, R.J. Mostert, Cold-pressing and vacuum arc melting of γ-TiAl based alloys, Adv. Powder Technol. 30 (2019) 2925-2939. https://doi.org/10.1016/j.apt.2019.08.038.

[24] S. Grasso, Y. Sakka, G. Maizza, Electric current activated/assisted sintering (ECAS): a review of patents 1906-2008, Sci. Technol. Adv. Mater. 10 (2009) 1-24. https://doi.org/10.1088/1468-6996/10/5/053001.

[25] R. Orru`, R. Licheri, A.M. Locci, A. Cincotti, G. Cao, Consolidation/synthesis of materials by electric current activated/assisted sintering, Mater. Sci. Eng. R 63 (2009) 127-287. https://doi.org/10.1016/j.mser.2008.09.003.

[26] Y. Garip, O. Ozdemir, A study of the cycle oxidation behavior of the Cr/Mn/Mo alloyed Ti-48Al-based intermetallics prepared by ECAS, J. Alloy Compd. 818 (2020) 1-14. https://doi.org/10.1016/j.jallcom.2019.152818.

[27] H.-W. Liu, K. P. Plucknett, Titanium aluminide (Ti-48Al) powder synthesis, size refinement and sintering, Adv. Powder Technol. 28 (2017) 314-323. http://dx.doi.org/10.1016/j.apt.2016.10.001.

[28] U. Anselmi-Tamburini, J.E. Garay, Z.A. Munir, Fundamental investigations on the spark plasma sintering/synthesis process III. Current effect on reactivity, Mat. Sci. Eng. A. 407 (2005) 24-30. https://doi.org/10.1016/j.msea.2005.06.066.

[29] Y. Garip, Investigation of the effect of alloying elements on oxidation and hot corrosion behavior of the Ti-48Al based intermetallics produced by electric current activated sintering method, Doctoral Thesis, (2019).

[30] J. Xua, J. Lang, D. Ana, J. Liua, Z. Hua, Z. Xie, A novel alternating current-assisted sintering method for rapid densification of Al_2O_3 ceramics with ultrahigh flexural strength, Ceram. Int. 46 (2020) 5484-5488. https://doi.org/10.1016/j.ceramint.2019.10.287.

[31] J.B. Yang, W.S. Hwang, The Preparation of TiAl-Based Intermetallics from Elemental Powders through a Two-Step Pressureless Sintering Process, JMEPEG 7 (3) (1998) 385-392. https://doi.org/10.1361/105994998770347837.

[32] H. Usman, A. F. Mohd. Noor, R. Astrawinata, The Effects of Cr and Mo on the Microstructure and Mechanical Properties of As-Cast TiAl Alloys, J. Eng. Technol. Sci. 45 (3) (2013) 294-306. http://dx.doi.org/10.5614%2Fj.eng.technol.sci.2013.45.3.6.

[33] Z. Nianlong, S. Zhiping, Effect of Cr on the Microstructure and Properties of High Nb-TiAl Alloys Prepared by Hot-pressing Sintering, International Conference on Materials Chemistry and Environmental Protection, (2016). https://doi.org/10.2991/meep-15.2016.1.

[34] L. Chena, H. Lan, C. Huang, B. Yanga, L. Du, W. Zhang, Hot corrosion behavior of porous nickel-based alloys containing molybdenum in the presence of NaCl at 750 °C, Eng. Fail. Anal. 79 (2017) 245-252. http://dx.doi.org/10.1016/j.engfailanal.2017.05.009.

[35] U. Anselmi-Tamburinia, J. R. Groza, Critical assessment electrical field/current application - a revolution in materials processing/sintering?, Mater. Sci. Tech. 33 (2017) 1855-1862. https://doi.org/10.1080/02670836.2017.1341692.

[36] J. M. Montes, F. G. Cuevas, F. Ternero, R. Astacio, E. S. Caballero, J. Cintas, Medium-Frequency Electrical Resistance Sintering of Oxidized C.P. Iron Powder, Metals 8, 426 (2018) 1-14. https://doi.org/10.3390/met8060426.

[37] Z. Trzaska, G. Bonnefont, G. Fantozzi, J.-P. Monchoux, Comparison of densification kinetics of a TiAl powder by spark plasma sintering and hot pressing, Acta Mater. 135 (2017) 1-13. http://dx.doi.org/10.1016/j.actamat.2017.06.004.

[38] M.A. Lagos, I. Agote, SPS synthesis and consolidation of TiAl alloys from elemental powders: Microstructure evolution, Intermetallics 36 (2013) 51-56. http://dx.doi.org/10.1016/j.intermet.2013.01.006.

[39] J. Zhu, W. Yang, H. Yang, F. Wang, Effect of Nb_2O_5 on the microstructure and mechanical properties of TiAl based composites produced by hot pressing, Mater. Sci. Eng. A 528 (2011) 6642-6646. https://doi.org/10.1016/j.msea.2011.04.062.

[40] E. Godlewska, M. Mitoraj, K. Leszczynska, Hot corrosion of Ti-46Al-8Ta (at.%) intermetallic alloy, Corros. Sci. 78 (2014) 63-70. http://dx.doi.org/10.1016/j.corsci.2013.08.032.

[41] Y. Qiao, J. Kong, X. Guo, Hot corrosion phenomena of Nb-Ti-Si based alloy and its silicide coating induced by different corrosive environments at 900 °C, Ceram. Int. 44 (2018) 7978-7990. https://doi.org/10.1016/j.ceramint.2018.01.238.

[42] M.M. Krolikowska, E. Godlewska, Hot corrosion behaviour of (γ+α_2)-Ti-46Al-8Nb (at.%) and α-Ti-6Al-1Mn (at.%) alloys, Corros. Sci. 115 (2017) 18-29. https://doi.org/10.1016/j.corsci.2016.11.006.

[43] M.-P. Bacos, A. Morel, S. Naveos, A. Bachelier-locq, P. Josso, M. Thomas, The effect of long term exposure in oxidising and corroding environments on the tensile properties of two gamma-TiAl alloys, Intermetallics 14 (2006) 102-113. https://doi.org/10.1016/j.intermet.2005.04.015.

[44] H. Jiang, J.-X. Dong, M.-C. Zhang, L. Zheng, Z.-H. Yao, Hot corrosion behavior and mechanism of FGH96 P/M superalloy in molten NaCl-Na_2SO_4 salts, Rare Met. 38 (2019) 173-180. https://doi.org/10.1007/s12598-016-0754-z.

[45] C. Leyensa, U, B. A. Pint, I.G. Wright, Effect of composition on the oxidation and hot corrosion resistance of NiAl doped with precious metals, Surf. Coat. Tech. 133-134 (2000) 15-22. https://doi.org/10.1016/S0257-8972(00)00878-1.

[46] Y.-H. QIAN, X.-C. LI, M.-S. LI, J.-J. XU, B. LU, Hot corrosion of modified Ti_3Al-based alloy coated with thin Na_2SO_4 film at 910 and 950 °C in air, Trans. Nonferrous Met. Soc. China 27 (2017) 954-961. https://doi.org/10.1016/S1003-6326(17)60111-0.

[47] F. Pettit, Hot Corrosion of Metals and Alloys, Oxid Met 76 (2011) 1-21. https://doi.org/10.1007/s11085-011-9254-6.

[48] J. A. Goebel, F. S. Pettit, G. W. Goward, Mechanisms for the Hot Corrosion of Nickel Base Alloys, Metall. Mater. Trans. B 4 (1973) 261-278. https://doi.org/10.1007/BF02649626.

[49] G. Sreedhar, V. S. Raja, Hot corrosion of YSZ/Al_2O_3 dispersed NiCrAlY plasma-sprayed coatings in Na_2SO_4-10 wt.% NaCl melt, Corros. Sci. 52 (2010) 2592-2602. https://doi.org/10.1016/j.corsci.2010.04.007.

[50] K. Zhang, T. Zhang, X. Zhang, L. Song, Corrosion resistance and interfacial morphologies of a high Nb-containing TiAl alloy with and without thermal barrier coatings in molten salts, Corros. Sci. 156 (2019) 139-146. https://doi.org/10.1016/j.corsci.2019.05.011.

[51] D. Mudgal, S. Singh, S. Prakash, Cyclic Hot Corrosion Behavior of Superni 718, Superni 600, and Superco 605 in Sulfate and Chloride Containing Environment at 900 °C, Metallogr. Microstruct. Anal. 4 (2015) 13-25. https://doi.org/10.1007/s13632-014-0182-0.

[52] M. Javidi, F. Bashtin, Investigating Hot Corrosion Behavior of SA 312 TP321H Stainless Steel and SA 335 P5 Ferritic Steel and Their Dissimilar Weldment in Corrosive Salt Environment, Oxid. Met. 89 (2018) 589-607. https://doi.org/10.1007/s11085-017-9803-8.

Figure List

Fig. 1. Schematic diagram of the resistance sintering apparatus and process conditions used in this study

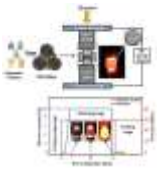

Fig. 2. XRD patterns of TiAl based intermetallics prepared by RS

Fig. 3. SEM images of the microstructures of the prepared intermetallics. Insets show higher magnification of the marked area.

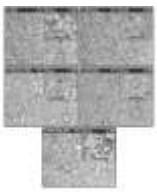

Fig. 4. Plots of weight change vs. time for hot corroded samples a) in wt. % Na_2SO_4-25K_2SO_4 melts at 900°C for 180 h b) in wt. % Na_2SO_4-25NaCl melts at 800°C for 180 h.

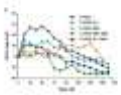

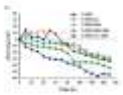

Fig. 5. XRD patterns of the hot corroded samples after hot corrosion for 180 h, a) in wt. % Na_2SO_4-25K_2SO_4 melts at 900°C and b) in wt. % Na_2SO_4-25NaCl melts at 800°C.

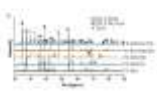

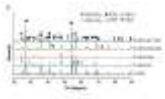

Fig. 6. SEM images of samples surface after corrosion in wt. % Na_2SO_4-25K_2SO_4 molten salts at 900°C for 180 h. Insets show higher magnification of the marked area. EDS analysis in marked spots (see Table 4).

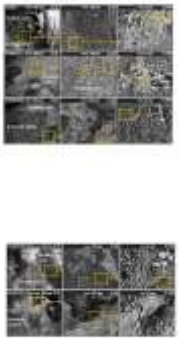

Fig. 7. SEM images of samples surface after corrosion in wt. % Na_2SO_4-25NaCl molten salts at 800°C for 180 h. Insets show higher magnification of the marked area. EDS analysis in marked spots (see Table 5).

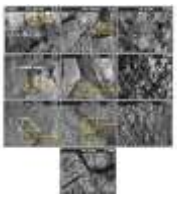

Fig. 7. Continued.

Fig. 8. Cross-section SEM images of samples after corrosion in wt. % Na_2SO_4-25K_2SO_4 molten salts at 900°C for 180 h. EDS analysis in marked spots (see Table 6).

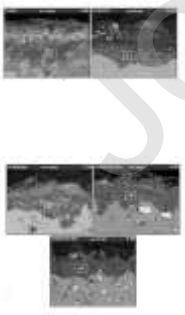

Fig. 9. Cross-section SEM images of samples after corrosion in wt. % Na_2SO_4-25NaCl molten salts at 800°C for 180 h. EDS analysis in marked spots (see Table 7).

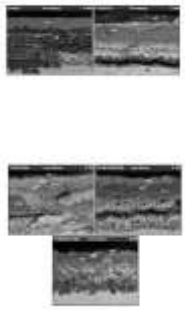

Fig. 10. Macrophotos of the samples after corrosion in wt. % Na_2SO_4-25K_2SO_4 molten salt at 900°C for 180 h.

Fig. 11. Macrophotos of the samples after corrosion in wt. % Na_2SO_4-25NaCl molten salt at 800°C for 180 h.

Fig. 12. A thermodynamic stability diagram for the Na-O-S system at constant temperature [29].

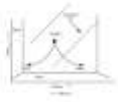

Fig. 13. Vapor pressures of possible chloride species formed by the reaction of NaCl with the studied samples in air, and vapor pressure for NaCl at 600-800°C (determined using HSC chemistry 6.0).

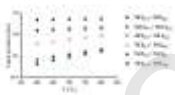

Table 1

Spot	Ti	Al	Cr	Mn	Mo

1	71.6	28.4	-	-	-
2	44.7	55.3	-	-	-
3	67.9	30.8	1.3	-	-
4	39.7	58.1	2.2	-	-
5	49.4	43.1	2.1	-	5.4
6	41.6	55.2	1.9	-	1.3
7	53.1	43.9	1.8	-	1.2
8	72.9	24.8	-	2.3	-
9	39.7	58.5	-	1.8	-
10	41.1	52.8	-	1.4	4.7
11	43.2	53.9	-	1.8	1.1
12	58.2	39.1	-	2.1	0.6

Table 2

Specimens	Experimental density (g cm-3)	Theoretical density (g cm^{-3})	Relative density (%)
Ti-48Al	3.82	3.88	98.45
Ti-48Al-2Cr	3.90	3.95	98.73
Ti-48Al-2Cr-2Mo	4.11	4.25	96.70
Ti-48Al-2Mn	3.92	3.97	98.74
Ti-48Al-2Mn-2Mo	4.13	4.26	96.94

Table 3

Specimens	Microhardness (HV)
Ti-48Al	344
Ti-48Al-2Cr	352
Ti-48Al-2Cr-2Mo	385
Ti-48Al-2Mn	347
Ti-48Al-2Mn-2Mo	377

Table 4

Spot	Ti	Al	Cr	Mn	Mo	O	Na	K
1	4.6	34.8	-	-	-	58.9	1.6	0.1
2	27.3	7.4	-	-	-	63.3	1.8	0.2
3	2.2	40.9	0.9	-	-	52.4	2.9	0.7
4	37.2	0.3	0.3	-	-	61.7	0.4	0.1
5	30.9	0.6	-	0.1	-	56.7	10.8	0.9
6	13.6	23.6	-	0.1	-	57.8	4.6	0.3
7	12.8	11.6	-	0.1	0.1	67.4	7.6	0.4
8	36.7	28.8	-	0.6	0.1	32.2	1.4	0.2
9	27.3	5.4	0.4	-	0.2	52.5	13.9	0.3
10	20.7	15.9	0.2	-	0.1	53.6	7.5	1.9

Table 5

Spot	Ti	Al	Cr	Mn	Mo	O	Na	Cl	S
1	32.4	2.8	-	-	-	58.9	2.1	2	1.8
2	13.3	14.6	-	-	-	49.1	19.9	2.5	0.6
3	23.8	1.3	-	-	-	54.6	17.4	0.9	1.7
4	28.3	3.9	0.1	-	-	64.8	2.4	0.2	0.3
5	32.7	5.2	0.1	-	-	43.8	16.9	0.1	0.2
6	26.2	0.2	-	0.1	-	48.3	16.4	8,5	0.3
7	27.7	5.5	-	0.1	-	56.3	8.9	0.6	0.9
8	25.6	6.7	-	0.1	0.1	59.5	2.5	3.3	2.2
9	19.6	8.9	-	0.1	0.4	56.4	9.9	2.8	1.9
10	16.7	7.9	0.2	-	0.2	53.2	17.8	3.4	0.6
11	25.8	3.7	0.1	-	0.1	60.2	3.4	3.8	2.9

Table 6

Spot	Ti	Al	Cr	Mn	Mo	O	Na	K
1	32.6	2.8	-	-	-	57.8	6.9	0.2
2	19.2	23.7	-	-	-	51.4	2.6	3.1
3	25.2	4.7	-	-	-	58.4	11.4	0.3
4	32.3	0.8	0.1	-	-	66.2	0.5	0.1
5	60.1	30.3	0.9	-	-	7.2	1.4	0.1
6	17.8	15.3	0.4	-	-	61.7	3.9	0.4
7	29.3	1.7	-	0.1	-	60.1	7.8	0.4
8	18.3	15.2	-	0.2	-	60.7	4.3	0.8
9	13.1	26.4	-	1.1	-	49.3	0.3	-
10	32.2	0.4	-	0.1	0.1	66.9	0.3	-
11	18.9	21.3	-	0.1	0.2	59	0.3	0.2
12	37.1	25.2	-	1.5	3.8	32.1	0.2	0.1
13	29.5	1.6	0.1	-	0.2	62.3	6.1	0.2
14	14.6	22.6	0.4	-	0.1	59.8	2.5	-
15	22.3	34.8	0.8	-	0.6	41.3	0.2	-

Table 7

Spot	Ti	Al	Cr	Mn	Mo	O	Na	Cl
1	34.1	0.4	-	-	-	61.7	2.1	1.7
2	25.8	13.5	-	-	-	37.3	5.6	17.8
3	30.1	19.4	-	-	-	24.7	15.6	10.2
4	30.1	3.7	0.2	-	-	52.8	9.9	3.3
5	27.9	3.2	0.8	-	-	62.8	3.1	2.2
6	3.8	40.6	0.4	-	-	52.7	1.6	0.9
7	25.9	15.8	2.3	-	-	50.4	0.9	4.7
8	55.6	38.7	1.1	-	-	4.4	0.2	-
9	25.3	1.6	-	0.1	-	61.8	10.1	1.3
10	32.1	2.9	-	0.5	-	61.4	2.7	0.4
11	21.3	1.3	-	0.6	-	54.2	14.8	7.8
12	0.4	1.9	-	-	-	5.2	40.8	51.7
13	2.6	44.9	-	0.1	-	49.6	2.7	0.1
14	58.8	11.9	-	0.8	-	26.4	0.6	1.5
15	25.7	1.7	-	0.2	-	57.7	13.1	1.6
16	32.3	2.1	-	0.3	0.1	64.3	0.3	0.6
17	3.5	46.5	-	0.1	0.2	49.5	0.1	0.1
18	33.3	19.4	-	2.2	1.2	39.9	0.4	3.6
19	51.6	33.1	-	2.4	0.6	9.6	0.2	2.5
20	39.2	1.3	0.1	-	0.1	51.5	7.4	0.4
21	31.8	3.1	0.3	-	0.1	62.4	2.3	0.1
22	4.1	40.7	0.4	-	0.2	52.3	1.9	0.4
23	30.8	3.2	0.6	-	0.1	62	2.1	1.2
24	49.5	1.2	0.2	-	0.1	29.8	11.4	7.8

Table 8

Reactions	ΔG^{o}_{25}	ΔG^{o}_{800}	ΔG^{o}_{900}
$Ti+O_{2(g)} = TiO_2$	-899	-750	-732
$4/3Al+O_{2(g)}=2/3Al_2O_3$	-1055	-891	-869
$2/3Mo+O_{2(g)}=2/3MoO_3$	-445	-317	-304
$4/3Cr + O_{2(g)} = 2/3Cr_2O_3$	-702	-569	-552
$Na_2SO_{4(s)} = Na_2O_{(s)}+SO_{3(g)}$	523	403	390
$2SO_{3(g)}= S_{2(g)} +3O_{2(g)}$	822	564	531
$3TiO_2 + Na_2O = Na_2Ti_3O_7$	-233	-225	-222
$Al_2O_3 + Na_2O = 2NaAlO_2$	-180	-171	-166
$Ti + Cl_{2(g)} = TiCl_{2(s)}$	-466	-344	-329
$2/3Ti + Cl_{2(g)} = 2/3TiCl_{3(s)}$	-436	-327	-314
$1/2Ti + Cl_{2(g)} = 1/2TiCl_{4(g)}$	-363	-316	-310
$2/3Al + Cl_{2(g)} = 2/3AlCl_{3(g)}$	-380	-352	-348
$1/2Mo + Cl_{2(g)} = 1/2MoCl_{4(g)}$	-177	-139	-134
$TiCl_{2(s)} + O_{2(g)} = TiO_2+ Cl_{2(g)}$	-424	-406	-403
$TiCl_{4(g)} + O_{2(g)} = TiO_2+ 2Cl_{2(g)}$	-163	-118	-112
$4/3AlCl_{3(g)} + O_{2(g)} = 2/3Al_2O_3 + 2Cl_{2(g)}$	-295	-186	-173

Table List